



# Micromechanical additive manufacturing and modeling of interdigitated capacitive touch sensors

Md Taibur Rahman<sup>a</sup>, Arya Rahimi<sup>b</sup>, Subhanshu Gupta<sup>b,\*</sup>, Rahul Panat<sup>a,\*</sup>

<sup>a</sup> School of Mechanical and Materials Engineering, Washington State University, Pullman, WA 99164, USA

<sup>b</sup> School of Electrical Engineering and Computer Science, Washington State University, Pullman, WA 99164, USA

## ARTICLE INFO

### Article history:

Received 25 January 2016

Received in revised form 23 May 2016

Accepted 14 July 2016

Available online 25 July 2016

### Keywords:

Aerosol Jet printing

Printed electronics

3-D printing

Wearable devices

Touch sensor

Electrostatic field simulations

Interdigitated capacitor

RC time constant

## ABSTRACT

Touch sensors have created a paradigm shift in the human-machine interaction in modern electronic devices. Several emerging applications require that the sensors conform to curved 3-D surfaces and provide an improved spatial resolution through miniaturized dimensions. The proliferation of sensor applications also requires that the environmental impact from their manufacturing be minimized. This paper demonstrates and characterizes interdigitated capacitive touch sensors manufactured using an Aerosol Jet based additive technique that reduces waste and minimizes the use of harmful chemicals. The sensors are manufactured with the capacitive elements at an in-plane length scale of about 50 μm by 1.5–5 mm, a thickness of 0.5 μm, and a native capacitance of a 1–5 pF. The sensor capacitance variation is within 8% over multiple samples, establishing the repeatability of the Aerosol Jet method. Scanning electron microscopy and atomic force microscopy are used to characterize the sensor electrodes. 3-D electromagnetic simulations are carried out to predict the capacitance of the printed sensors and the electric field distribution. The simulations show a reasonable agreement with the experimental values of the sensors' native capacitance (within 12.5%). The model shows the native capacitance to be relatively insensitive to the thickness of the sensor electrodes, allowing touch sensors to be fabricated with reduced material usage and cost. The model is further used to establish the important sensor dimensions governing its electrical performance. Lastly, electromagnetic field distribution predicted by the model is used to establish the physical range of the touch action to be about a millimeter out of the plane of the sensors for the geometries considered in the current work.

© 2016 Elsevier B.V. All rights reserved.

## 1. Introduction

Wearable 'smart' electronic devices are projected to bring transformative changes to the global economy over the next two decades, with an associated economic value projected to be in the trillions of dollars by 2020 [1,2]. Touch sensors form the most important type of human-machine interaction for such devices with important uses in defense applications, robotics [3], and healthcare [4]. The electronic circuit enabling the touch sensors works largely through detecting the changes in input capacitance by incorporating the distinction between varied stimuli such as stylus, single/double/multiple touch, and touch duration [5]. Although such sensors are already in use, several Internet of Things (IoT) applications have added requirements for size and conformabil-

ity of the sensors per the location of the sensor circuit. In addition, with an increase in the number of wearable devices, the environmental impact of the manufacturing of its constituents is expected to be significant [6] and requires concerted development of green manufacturing techniques.

To date, several attempts have been made to fabricate low-cost capacitive touch sensors (or touch panels) for various applications. A flexible capacitive sensor with encapsulated liquids as the dielectrics was demonstrated using a MEMS-based manufacturing method [7]. A capacitive touch interface for RFID tags was demonstrated, also using a MEMS-based method [8]. A stretchable capacitive sensor made of thin gold film on silicone rubber was fabricated using photolithography and characterized [9]. A capacitive touch panel using metalized paper was demonstrated with an effective capacitance of about 50 pF [10]. A foldable direct write paper-based capacitive touch pad was developed using inkjet printing of silver nanowires at a feature scale of 500 μm and a capacitance range from 2 to 40 pF [11]. This work [11], however, did not report the resistivity of the sintered nanowires, a criti-

\* Corresponding authors.

E-mail addresses: [sgupta@eecs.wsu.edu](mailto:sgupta@eecs.wsu.edu) (S. Gupta), [\(R. Panat\)](mailto:rahul.panat@wsu.edu).

cal parameter for power consumption in IoT devices/applications [12–14].

In contrast to the conventional subtractive or semi-additive MEMS-based fabrication techniques, additive techniques such as Aerosol Jet Method (AJM) [15] are being developed to fabricate passive structures. Such methods avoid creating material waste. The AJM also requires considerably less amounts of environmentally harmful chemicals compared to the MEMS-based techniques. The AJM utilizes a mist of nanoparticle inks directed by a carrier gas to print features at a length scale of 10  $\mu\text{m}$  over a flat or a curved surface and has been used to manufacture solar cells [16,17], electronic interconnects [18], biosensors [19], strain sensors [20,21], and 3-D antenna structures [22]. The maximum particle size in the inks used in the AJM is typically <500 nm [23], with the sintering of the nanoparticles achieved at a temperature significantly lower than the bulk melting point. The conductivity obtained by such methods is about 20–50% of the bulk metal [22]. The AJM has also been shown to allow a standoff height (i.e., vertical distance between the nozzle printing the ink and the substrate) up to 5 mm, enabling electronic circuits on complex 3-D surfaces [22,23].

Although several manufacturing routes have been explored for touch sensors, few if any electromagnetic simulations have been carried out to predict their native capacitance and performance as a function of the sensor electrode morphology, dimension, and the surrounding dielectric medium. Finally, a complete design tool with simulations and predictive modeling integrated with manufacturing could enable rapid prototyping and development of custom-sensors at minimal costs. In addition, the sensor manufacturing variability and its effects on the sensor electrical characteristics have not been reported comprehensively in the literature for additive manufacturing techniques.

The present work demonstrates and characterizes printed capacitive interdigitated touch sensors using an Aerosol Jet micro-additive manufacturing technique with the native sensor capacitance in the range of 1–5 pF. The manufacturing method is shown to allow sensor feature sizes down to tens of microns, with a capacitance per interdigitated electrode-pair of about 100 fF. Section 2 describes the sensor operating principle, while Section 3 provides a detailed experimental procedure of sensor fabrication by the Aerosol Jet printing. Section 4, along with Supplementary information S1–3, provides details of 3-D electrodynamic model developed to predict the capacitance of the printed sensors. The sensor measurements are described in Section 5, while the results are presented and discussed in Section 6.

## 2. Sensor operating principle

The schematic of the design and the operating principle of the sensor is shown in Fig. 1. The sensor consists of an interdigitated electrode structure forming the capacitor with the probe pads connected using interconnects (Fig. 1-a). Fig. 1-b, c shows the expected field lines in the untouched state and the schematic of an equivalent electrical circuit, respectively. The coupling between the two sides of the capacitor is expected to occur through air as well as through the glass base. Fig. 1-d, e, shows the expected field-line disruptions (in air) when touched by a thumb and the schematic of its equivalent circuit with the added capacitance,  $C_{\text{touch}}$  due to the high relative permittivity of the skin/tissue/blood ( $\epsilon_r$ ), respectively. Note that a thin layer of non-conductive plastic over the sensor prevents the thumb from shorting the capacitor and will be considered in simulations.  $C_{\text{touch}}$  acts in parallel to the capacitance,  $C_0$ , in the untouched state, resulting in the total capacitance,  $C_{\text{sensor}} = C_0 + C_{\text{touch}}$ . Electromagnetic simulations were developed to determine the field lines outside the sensor plane and determine

the field disruption when touched. These simulations also enabled estimating the expected capacitances prior to fabrication.

## 3. Sensor fabrication

An Aerosol Jet micro-additive manufacturing machine (AJ300, Optomec Inc, Albuquerque, NM, USA) was used to print the electrodes directly onto the glass substrate as shown in Fig. 2 (also see Fig. S1 for a picture of the equipment). An ultrasonic atomizer was used to create the aerosol/mist. The nozzle exit diameter during printing was 150  $\mu\text{m}$ , while the atomizing flow rate and the sheath gas flow rate were maintained at 25 sccm and 50 sccm, respectively. During printing, the standoff distance between the substrate and the nozzle was kept at about 2.8 mm. Note that the optimized parameters such as sheath gas pressure, atomizing pressure and exhaust pressure were suitable for the ink formulation used in the current work but may vary for other inks depending upon their viscosity, particle size and the solvent type.

The electrodes were printed using a silver nanoparticle ink (Perfect-TPS G2, Clariant Group, Frankfurt, Germany) with a viscosity of about 1.5 cP, a particle size of 30–50 nm and a particle loading of  $40 \pm 2$  wt%. A transparent glass slide (Thermo Fisher Scientific, Waltham, MA, USA) was used as the substrate. The substrates were cleaned with DI water followed by isopropyl alcohol. The substrate surface was then further treated with an atmospheric plasma (Atomflo™ 400, Surfx® Technologies LLC, Redondo Beach, CA, USA) at 100 W for 5 min. Before printing the structures, ink material was placed in a tube which was rotated continuously around its axis for 12 h using a tube roller (Scilogex MX-T6-S, Rocky Hill, CT, USA) at about 70 rpm to prevent nanoparticle agglomeration within the ink. The printed material was then sintered at 200 °C for 30 min in a programmable oven (Neytech Vulcan furnace, Model 3-550, Degussa-Ney Dental Inc., Bloomfield, CT, USA) to create conductive electrodes. The electrode resistivity was measured through a 4-Wire method and was about  $6.35 \times 10^{-8} \Omega\text{-m}$ , or about 5X of the bulk silver and within the range reported in literature for thermally sintered nanoparticles of silver [24]. Three sensors were fabricated for each of the interdigitated region lengths of 1.5, 3, and 5 mm. For the samples with 3 mm interdigitated region length, a sensor with smaller number of electrodes (8) was also fabricated.

## 4. Sensor simulation methodology

Consistent use of additive printing (e.g. by Aerosol Jet method) will require an accurate and well-modeled parametric library of the different variables involved. Electromagnetic simulations can be used to study the effect of various geometrical and material parameters on the sensor behavior to aid in its design. The simulations can also provide a quantitative picture of the electric field for the sensor geometry to further illustrate its behavior under different conditions. We used the Momentum ADS® and EMPro® software (Keysight®, Santa Rosa, CA, USA) in this work to develop detailed 3D models and simulation structures for the printed touch sensors. A 2D layout was created in Momentum ADS® and then exported to EMPro for simulation with additional 3D components using a frequency-domain finite element method (FEM) solver. The added 3D electromagnetic (EM) components enabled detailed study of the electric fields to understand different aspects of manufacturability and electrical behavior of the printed sensors. Both programs are 3-D planar electromagnetic simulators used for passive circuit analysis with partial differential equation solvers for Maxwell's equations (with boundary conditions prescribed by the users) based on the method of moments [25,26]. Each model took into consideration internal and external parasitics, surface roughness and variations in metal thickness, dielectric constants, and

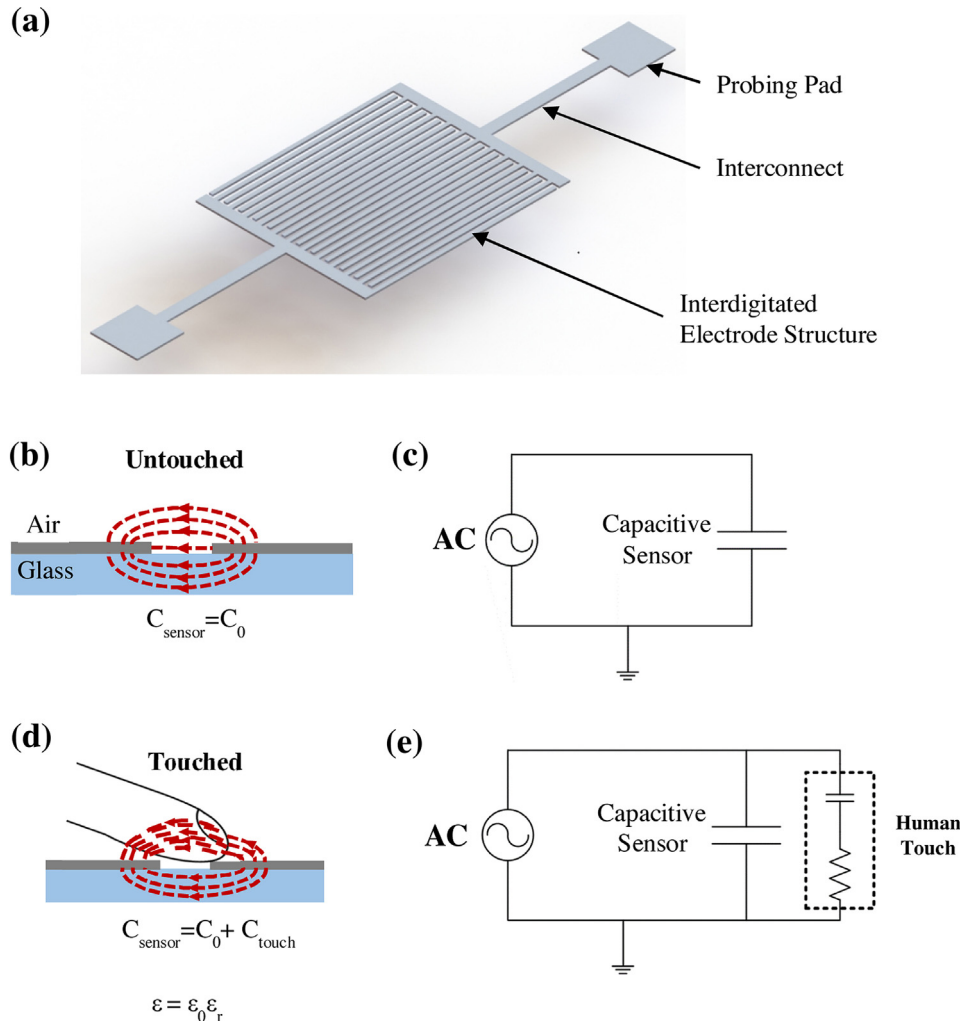


**Fig. 1.** Operating principle of a capacitive touch sensor. (a) Schematic 3D view of the sensor, (b) schematic of the working principle of untouched sensor, (c) equivalent circuit of the untouched sensor, (d) schematic of the working principle of touched sensor. Here,  $\epsilon_0$  is the permittivity of free space ( $8.85 \times 10^{-12} \text{ F/m}$ ),  $\epsilon_r$  is the relative permittivity of human skin ( $\sim 40$ ), and  $\epsilon$  is the effective permittivity; and (e) equivalent circuit of the touched sensor.

detailed design parameters. A separate 3D model was created for each electrode number and length and was characterized in detail. The simulation details, including the dimensions, parameters, meshing techniques as well as illustrations of the sensor action with and without the touch and field line simulations are described in Supporting information S1–3.

## 5. Sensor measurements

An LCR meter (E4980, Agilent Technologies, Santa Clara, CA USA) was used to measure the capacitance of an untouched printed sensor as shown in Fig. 3. The samples were grounded to a metallic base connected to the LCR meter to minimize ground loops and improve accuracy. Proper “open” and “short” calibrations were done prior to taking the measurements. Calibration times were set to ‘long’ to allow precise calibration. A test fixture for the LCR meter (Model 16047A, Agilent Technologies, Santa Clara, CA USA) was used to convert the 4-terminal I/O into a 2-terminal I/O. Efforts were made to calibrate the probing wires to the measuring pads of the capacitor structure to de-embed any external parasitics. Parasitic stray admittances and residual impedances from the interconnects and the capacitor pads to the LCR meter were compensated using ‘OPEN’, ‘SHORT’ and ‘LOAD’ correction steps in the LCR meter.

Conventional solders have a high melting temperatures and need to use flux, which can affect the printed pads on the sensor. In addition, a soldering gun could not be used as it was observed to easily damage the printed structures. To circumvent these problems, we used a low melting temperature solder alloy, 52In-48Sn (Indium Corporation of America, Clinton, NY, USA) which is used for low temperature soldering in microelectronics [27], to interface with the printed structures. Small bits of the indium-based solder, each with a size of the order of  $1 \text{ mm}^3$ , were manually placed on the measuring pad and then melted using a temperature controlled hot air gun set to about  $180 \pm 10^\circ\text{C}$ . The measured solder resistivity ( $\rho_{\text{solder}} = 8.07 \times 10^{-7} \Omega\text{-m}$ ) was found to be an order of magnitude higher than the resistivity of the electrodes. The higher resistivity of the solder is expected to result in a lower quality factor for the capacitor but is not expected to affect the sensor functionality in the sub-MHz frequency range. The testing apparatus for a representative sensor is shown in Fig. S5.

During measurements it was found that the LCR meter did not provide correct readings when the sensor is ‘touched’ with a dry thumb (wrapped with an insulating material) due to system auto-correction as discussed in Supporting information (see Section S-4). The sensor response to the touch action was demonstrated using a RC circuit and captured on a Tektronix TDS5104B Digital Phosphor Oscilloscope. A  $300 \text{ kHz } 1V_{\text{pk-pk}}$  50% duty cycle square-wave was

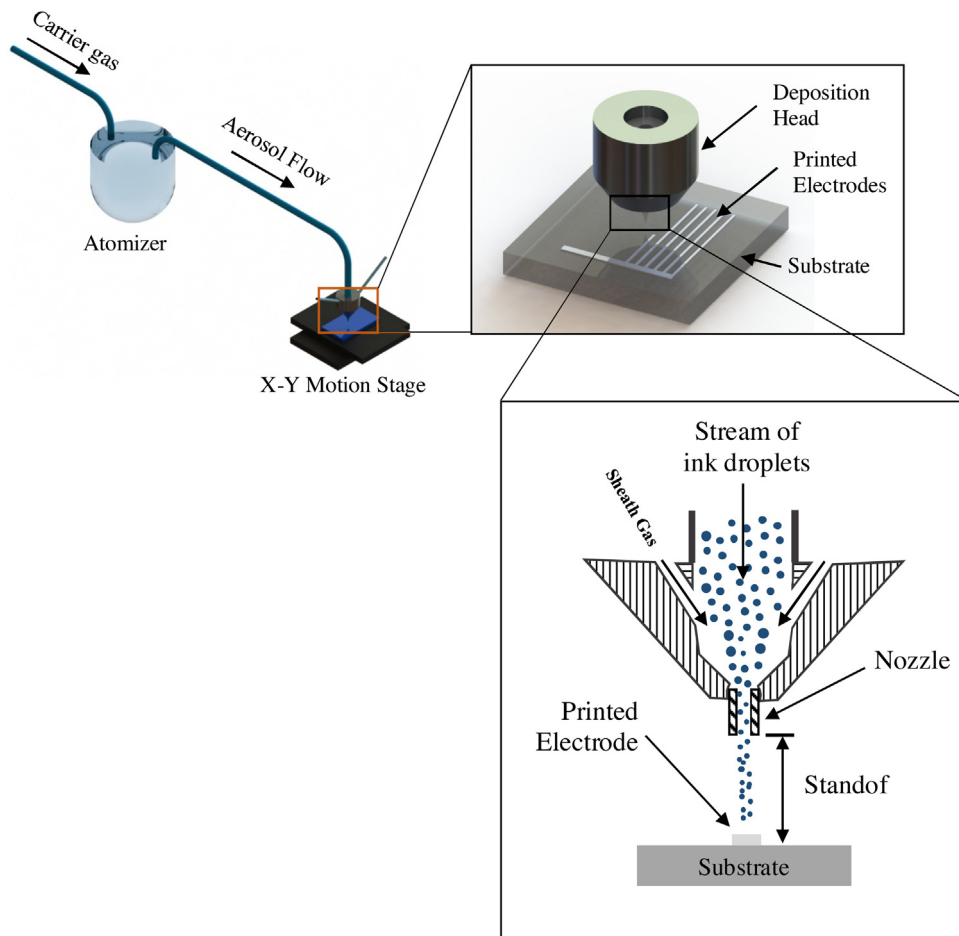


**Fig. 2.** Schematic of an Aerosol Jet system along with the fabrication process of capacitive sensor.

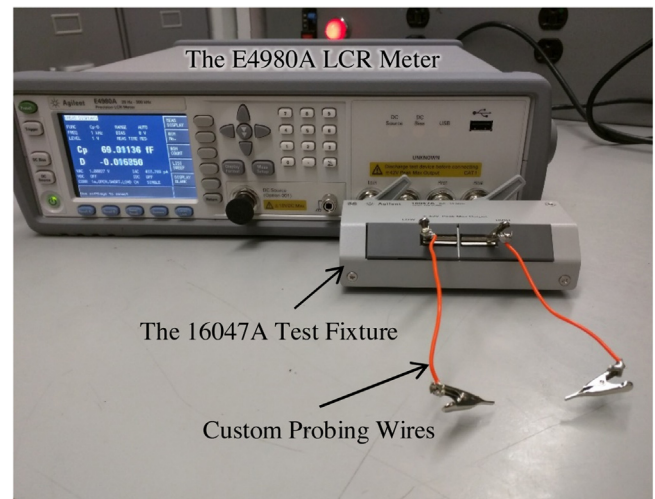
applied to a series resistor connected in shunt to the capacitive sensor under test. Three repeated measurements were carried out by the same individual for a sensor each with the interdigitated overlap lengths of 1.5, 3, and 5 mm, using this setup. The time constant was measured based on  $\tau = \frac{t_{90\%} - t_{10\%}}{2.2}$  (% is based on signal rise time). The time constants for the touched and untouched state were used to obtain the ratio of the capacitance in the touched state to that in the untouched state. This ratio along with the untouched capacitance from the LCR meter were used to get the sensor capacitance in the touched state.

## 6. Results and discussion

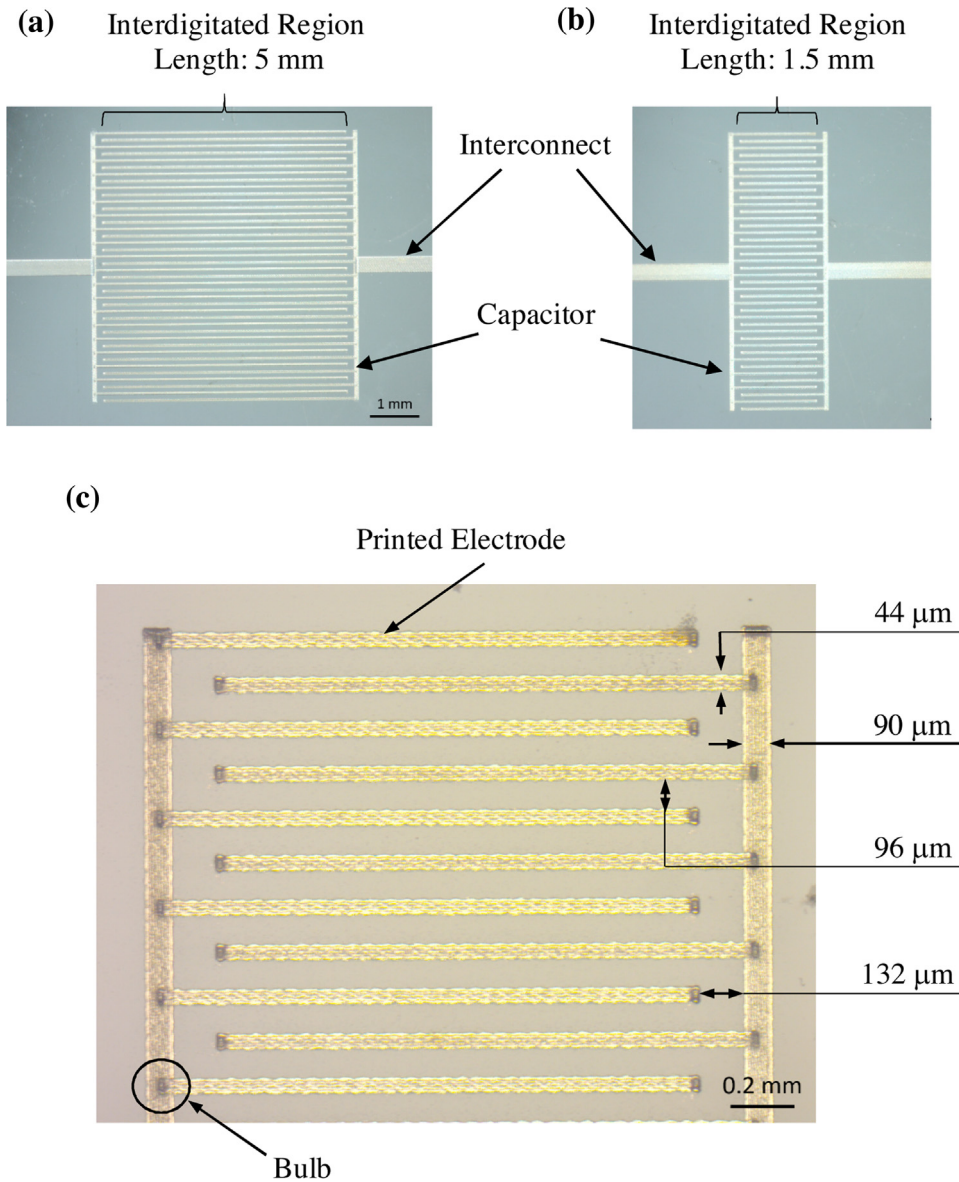
### 6.1. Printed electrode morphology

Fig. 4-a–c shows optical images of the capacitive sensors fabricated over a glass substrate using the Aerosol Jet technology with interdigitated region length of 5 mm (Fig. 4-a) and 1.5 mm (Fig. 4-b) and a total of 40 electrodes (20 per side) per sensor. Fig. 4-c shows a higher magnification image of one representative printed sensor electrode with dimensions. Prior to printing the structure, the sensor schematic was fed to the printer using the software AutoCAD 2015 (Autodesk Inc., San Rafael, CA, USA) with dimensions provided by the electromagnetic simulations (discussed in the next section). In addition to varying the electrode length, some sensors were fabricated with simple variations to the original drawing, to assess the effect on the capacitance and sensitivity. Note that the sensor electrodes also show the formation of a ‘bulb’ at the termination and at the overlap of the electrodes and connecting lines.

The bulb formation can be controlled by the shutter speed of the deposition head of the printer. The effect of bulb formation on the function of the sensor is expected to be minimal as it merely adds to the thickness of the printed electrodes in a confined area. This assumption is supported by simulations, where the sensor capacitance will be shown to be relatively insensitive to the electrode thickness (Section 6.3). The interdigitated region was printed using a single layer of deposited ink with individual electrodes formed by



**Fig. 3.** Agilent LCR meter test setup.



**Fig. 4.** Optical images of the printed capacitive touch sensor with (a) electrode length of 5 mm, (b) electrode length of 1.5 mm, and (c) high magnification image of the sensor in (b).

multiple lateral (i.e. side-by-side) passes, while the electrical connection pads were printed using at least 4 layers of printed ink to allow enough mechanical strength for solder connections to the external circuit. Fig. 5-a shows the SEM image of the printed electrode after thermal curing, along with higher magnification inset. The images clearly show surface features at an in-plane length scale of  $\sim 1 \mu\text{m}$ . The appearance of the printed electrode surface is highly 'rugged' as expected from a direct-write printing process, in contrast to the smooth surfaces obtained by other fabrication techniques such as electroplating [28]. The electrode surface profiles after sintering as measured under an Atomic Force Microscope (Dimension Icon, Bruker Corporation, Billerica, MA, USA) are shown in Fig. 5-b–d. Fig. 5-b shows the profiles for the same electrode at different locations along its length, while Fig. 5-c, d show the profile of two additional electrodes. The average electrode thickness is about  $0.5 \mu\text{m}$ , with a thickness varying between  $0.2 \mu\text{m}$  and about  $1.7 \mu\text{m}$ . This thickness variation is high and its effect on the sensor native capacitance and the capacitive action are discussed later in this section. Note that the observed surface roughness could be

lowered to  $\pm 100 \text{ nm}$  range by increasing the number of passes to about ten [22]. In the current study, we kept the number of passes to one for speed of the manufacturing and to reduce the material consumed per sensor. A measurement of 15 electrodes under an optical microscope shows a width of  $44.3 \mu\text{m}$  and a variation of  $\pm 2.58 \mu\text{m}$ , or 5.8% of the electrode width. The variation in the electrode width along a single electrode was comparable to that observed over multiple electrodes, indicating good repeatability of the printing process by the AJM.

## 6.2. Electric field

Fig. 6-a,b shows the equivalent simulated E-field captured with the vertical- and horizontal-planar sensors respectively for an interdigitated structure with a total of 19 electrodes (sensor being symmetric about one axis parallel to the length of the electrodes). The color patterns describe the intensity/strength of the E-fields changing from red to purple as fields becomes weaker. The E-field patterns show some asymmetry in the z-direction which can be

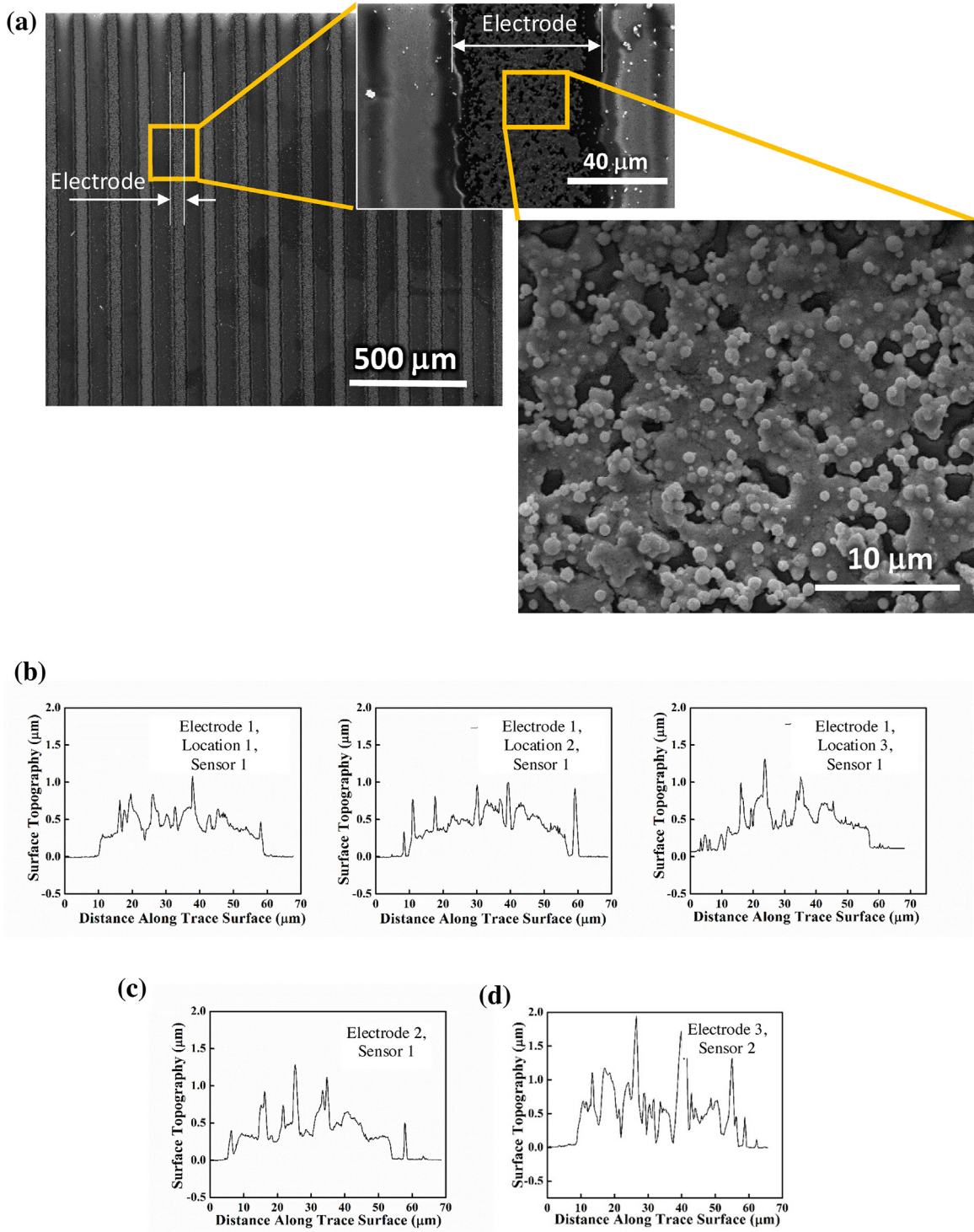


**Fig. 5.** (a) Representative SEM images of sensor electrodes under different magnifications showing a texture created by sintered nanoparticles. (b) Representative AFM scans of a single electrode at three different locations, (c) AFM scan of an electrode from the same device as (a), and (d) AFM scan of an electrode from a different device.

attributed to the coupling through the glass substrate on one side and air on the other. The reason for the asymmetry in the plane of the sensor is not clear at this time but is speculated to be due to the imperfections of EM mesh generated by the software for the high aspect ratio electrodes (Fig. S3). The simulations show that the electric field extends to about 2 mm into the space above and below the sensor (about 1 mm above the sensor top surface and about 1 mm below the sensor bottom surface) allowing the touch action to be effective even if an external object with a different dielectric is not

touching the sensors but is present within the field. This characteristic can also be useful for proximity sensing [29] applications. Note that Fig. 6-a also shows that the field is negligible in the plane of the sensor but outside the sensor area, suggesting that the probe pads and the interconnect lines joining the pad with the electrodes do not significantly contribute to the system capacitance. It is interesting to note that the classical solution of a pair of parallel plate capacitors shows that the electric field is confined within the parallel Plates [30]. The results for the interdigitated/comb geometry in

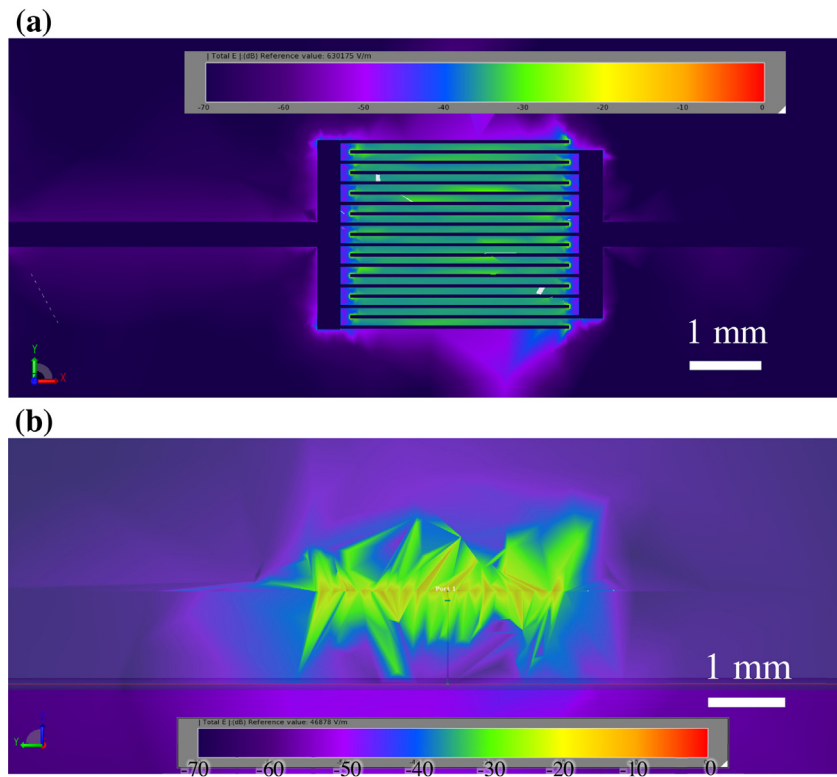


**Fig. 6.** Simulated electric field of the capacitive sensor (a) Top electric field in dB (reference electric field,  $E$ , 630175 V/m), (b) Planar electric field in dB (reference electric field,  $E$ , 46878 V/m).

the current study (Fig. 6-a), show that the electric field is confined within the plane of sensor. The out-of-plane electric field, however, is not confined by any physical features of the sensor (Fig. 6-b) and is expected to be a function of the electrode width and gap.

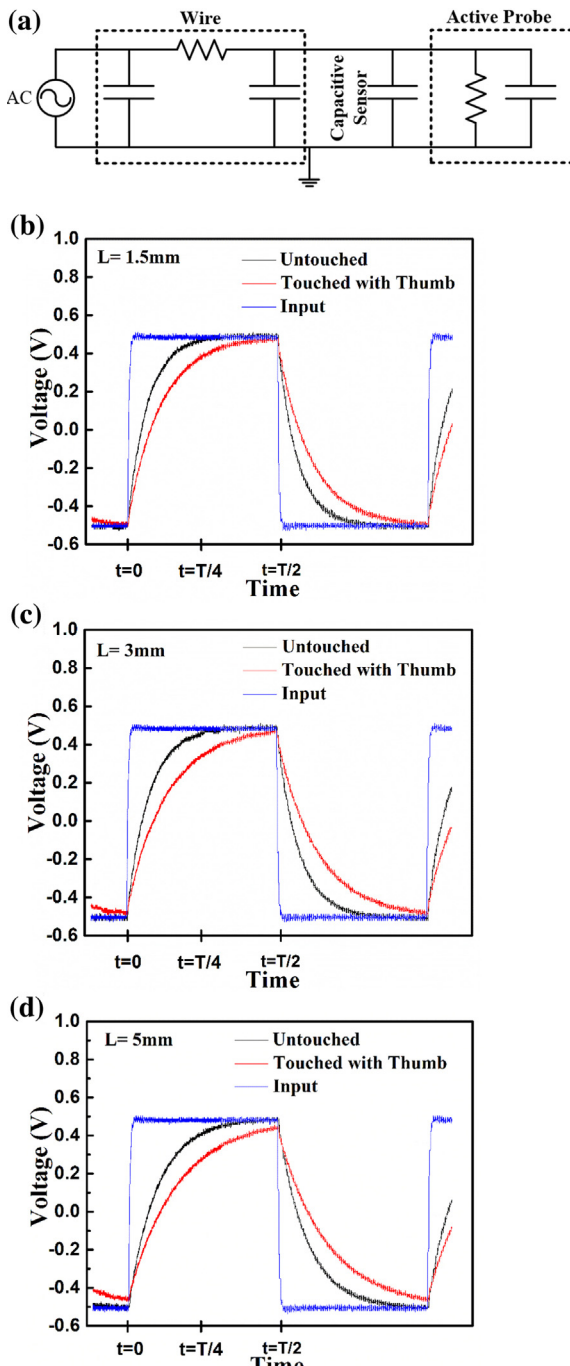
### 6.3. Capacitance measurements and simulations

For the sensor in the touched state, the equivalent electrical schematic and the response of the RC circuit (for both untouched and touched cases) captured from the oscilloscope for capacitors with 1.5 mm, 3 mm, and 5 mm interdigitated region length is shown in Fig. 7-a-d, respectively. A delay in the rise time for the touched state can be compared to that in the untouched state to get the ratio of the capacitance in the respective states. The ring-up and ring-down time constants for the RC circuit response in Fig. 7-b-d, are given in Table S2. The ratios of the touched to the untouched time constant for the rise and the fall cycles are within 9% and this difference was attributed to the parasitics in the oscilloscope connectors which could not be calibrated out during time constant measurements. Note that the capacitance value in the touched state was measured using the LCR meter as described in Section 5.

The sensor capacitance in the untouched state as a function of the interdigitated region length as measured from the LCR meter (with each sensor having a total of 40 electrodes or 20 electrode pairs) is shown in Fig. 8-a. Each data point represents an average and standard deviation of three samples. The measured untouched capacitance showed a very low standard deviation (maximum  $\pm 8\%$  of the mean) indicating good reproducibility of the AJM. The capacitance linearly increased with the interdigitated region length. In order to get the effect of the number of electrode pairs on the capacitance, an additional sample of 3 mm interdigitated region length was fabricated with 8 electrode pairs. The measured capacitance as a function of electrode pairs is shown in Fig. 8-b. The simulated capacitance using Momentum ADS® are also shown in

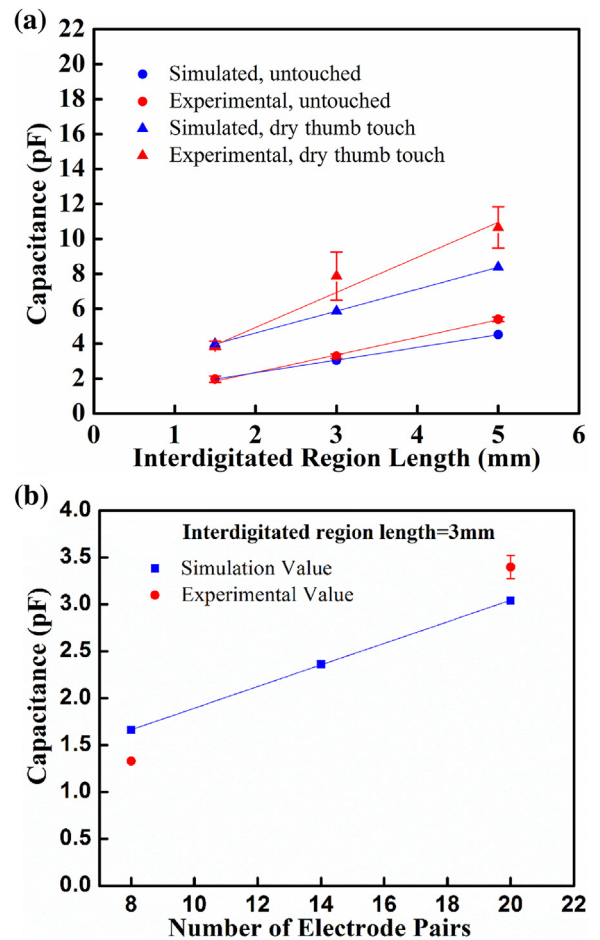
Fig. 8-a, b and confirm the linear increase in the sensor capacitance with length of the interdigitated region. Further, the simulations also predict that the sensor capacitance linearly increases with the numbers of interdigitated electrode pairs. In Fig. 8-a, the difference between the simulated values and the measured values of the capacitor is the lowest for the smallest capacitor, and increases with the capacitor length to  $\pm 12.5\%$ , a reasonable agreement. The increase in the deviation between the modeling results and the experimental measurement with the interdigitated region length is not entirely clear but thought to be due to the relatively higher parasitics for the longer capacitor. The agreement of the simulated capacitance of the sensor with the experimental values shown in Fig. 8-a, b is remarkable given the actual thickness variation of the electrodes (e.g. Fig. 5-b-d). An explanation of this observation is based upon further modeling results as discussed later in this section. The data used to plot Fig. 8-a, b is given in Table S3.

Fig. 8-a also shows the effect of dry thumb touch on the interdigitated capacitor, covered with a sheet of polystyrene. The touched capacitance shows a  $\sim 2X$  increase over the untouched state. The standard deviation in the measured capacitance in the touched state comes from three repeated measurements by the same individual. Simulated values of the thumb touch (assuming  $\epsilon_r = 40$ ) capture the trend observed in experiments. The difference between the measured and simulated values is higher in the touched state, with the difference increasing with the length of the interdigitated region of the capacitor. Note that the R-C measurement technique does not account for any parasitic resistance or capacitance due to the external leads connected to the equipment and is also affected by the angle of thumb placement, surface area of the thumb, tissue thickness and thumb pressure. At this time, the objective of the current work was to demonstrate the sensor design and characterize the sensor action through simulations; a complete study with different human subjects along with skin thickness and thumb pressure will be part of a future investigation.



**Fig. 7.** (a) Equivalent electrical schematic for the measurement of RC time constant. (b-d) RC time constant plots for sensors with an interdigitated region length of 1.5 mm, 3 mm, and 5 mm, respectively. The x-axis is plotted for one time period. The ring up and ring down time constants are given in Table S2.

**Fig. 9-a** shows the simulated capacitance for electrode thickness from 1  $\mu\text{m}$  (current study) to 100  $\mu\text{m}$ . The results reveal that a two orders of magnitude increase in the thickness results in only 20–30% increase in the sensor capacitance. In other words, the capacitance is relatively insensitive to the sensor thickness, allowing a set of electrodes with high thickness variability (see AFM images in **Fig. 5-b-d**) to produce a low variation in the sensor capacitance (error bars for untouched capacitance in **Fig. 8-a**). This result can be well understood from the EM field line patterns (**Fig. 7**). The capacitive coupling occurs over two millimeters in air and in glass which is at a length scale much larger than the electrode thickness



**Fig. 8.** (a) Experimental and simulated values for the variation of capacitance with interdigitated region length for touched as well as untouched state. (b) Experimental and simulated values of the effect of number of electrodes on the capacitance of a touch sensor with interdigitated region length of 3 mm.

of  $<2 \mu\text{m}$ . This result also has two important consequences from manufacturing perspective. First, since the direct-write printing processes require several passes to build up the electrode thickness, the above result indicates that a sensor with a very thin electrode built by a single pass printing will not have a very different native capacitance and electric field distribution when compared to those built with multiple passes. This is expected to have significant benefit to manufacturing as the number of passes proportionally increase the manufacturing time [23] and hence the cost [31]. Secondly, the behavior of touch sensors is expected to be relatively insensitive to the non-uniformity in the electrode thickness, thus saving the cost of quality control [32] of such sensors.

**Fig. 9-b** shows simulated values of capacitance as a function of electrode width,  $W$ , of the touch sensor, expressed as a% of the pitch of the interdigitated pattern of the sensor (dimension  $(W+G)$  in the inset of **Fig. 9-b**) for a sensor with 5 mm interdigitated region length. Twenty electrode pairs (a total of 40 electrodes) were used in the simulation. Further, two values of  $(W+G)$  are considered, namely, 225  $\mu\text{m}$  and 100  $\mu\text{m}$ . In both the cases, the sensor capacitance increases with an increase in  $W$  for a given electrode pitch  $(W+G)$ . However, the increase in capacitance is not uniform and divided into three separate regions. In region 1, the sensor native capacitance increases rapidly for  $W$  values from zero to about 2.5%. The capacitance then increases at a slower rate in region 2 until  $W$  is about 90% of the pitch  $(W+G)$ . In region 3, as  $W$  approaches the pitch  $(W+G)$ , i.e. when the gap between the electrodes is small, the capacitance increases rapidly. Overall, an increase in  $W$  by a

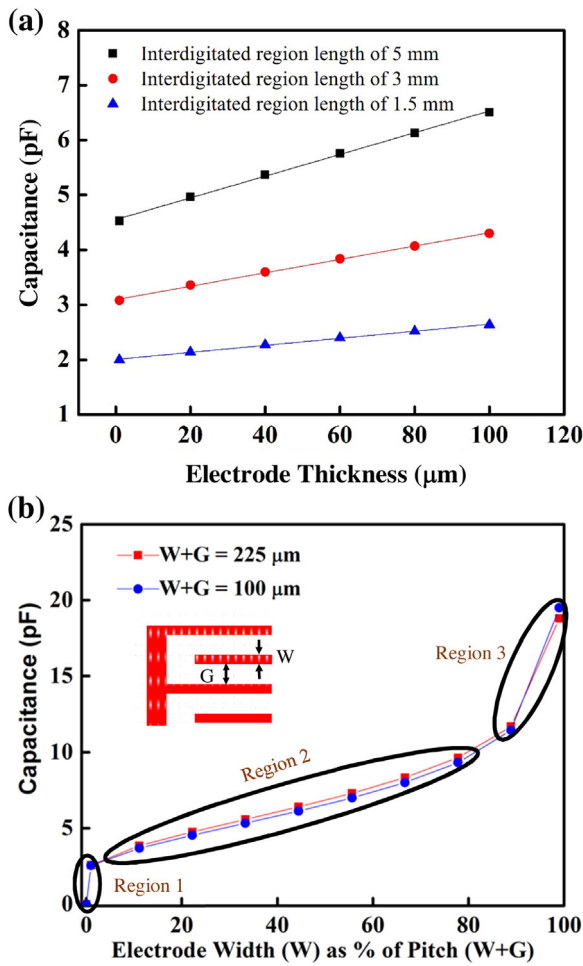


**Fig. 9.** (a) Simulated value of capacitance as a function of electrode thickness for three interdigitated region length values. (b) Simulated value of capacitance as a function of electrode width,  $W$ , expressed as a % of pitch ( $W+G$ ) for a touch sensor with interdigitated region length of 5 mm. The capacitance response is divided into three regions indicated on the figure. In region 1, the sensor native capacitance increases rapidly until  $W$  is about 2.5% of the pitch ( $W+G$ ). The capacitance then increases at a slower rate in region 2 until  $W$  is about 90% of the pitch ( $W+G$ ). In region 3, as  $W$  approaches the pitch ( $W+G$ ), i.e. when the gap between the electrodes is small, the capacitance increases rapidly again.

factor of 49 for a given pitch ( $W+G$ ) is shown to increase the simulated capacitance by a factor of 10. This sensor behavior can be understood from the fact that majority of the capacitive coupling happens through the electric field lines out of the plane of the sensor rather than in the in-plane gap between the electrodes (Fig. 7-a, b). Several additional features of Fig. 9-b that are not clearly seen from the graph should be noted. As expected, the predicted sensor capacitance is zero when  $W$  reduces to zero. On the other hand, as  $W$  approaches the pitch ( $W+G$ ), the gap between the electrodes approaches zero and the sensor capacitance increases to very high values and is expected to approach asymptotically to infinity. At  $W$  equal to the pitch ( $W+G$ ), however, the sensor shorts and the capacitance will be zero. Fig. 9-b also shows that the native capacitance of the touch sensor is dictated by the  $W$  as a % of ( $W+G$ ) more than the actual value of  $W$ , an observation highly useful in designing miniaturized sensor arrays. The results in Fig. 9-b can guide the manufacturing processes as well. For example, the touch sensor should be designed such that the electrode/gap dimensions should be in region 2, to avoid a small variation in the width of the electrodes (as expected from printing or lithographic processes) to lead to a high variation in the capacitance of the touch sensor (e.g. as in regions 1 or 3). The modeling data of the region 2 also shows the

quantitative variation in the capacitance change with the change in the electrode width for a given electrode pitch.

The experimental and modeling results presented in the paper provide a useful framework to design and additively manufacture capacitive touch sensors with feature length scale down to  $\sim 50 \mu\text{m}$ . The touch sensor can be printed anywhere, including over a curved, angled surfaces (see Rahman et al. [22]) such as a Si chip or an electronic package, making an integration of on-chip capacitor at arbitrary locations a possibility. The results also indicate that a single layer of the sensor electrode can suffice to give adequate sensor action at the frequencies considered in the current work and typically required for IoT applications. It is also important to consider the limitations of the current study. First, the additive method involves serial writing and hence can only be scaled up to high volumes by adding the number of print-heads working in-tandem for printing over a large area. Indeed, such efforts are taking place in the industry with 4-printheads being used in production for Aerosol Jet technology. In case of inkjet printing, the number of print heads per equipment is very large, however, the manufacturing accuracy and resolution is not as good as Aerosol Jet technology [21,22]. Secondly, the proposed fabrication technique, although suitable for low frequency applications, can result in considerable resistive losses due to skin-effect at high frequencies. This problem can be circumvented by printing multiple layers that reduces the surface roughness [22], but results in an increase in the time required for printing and also increases material consumption. The simulations presented in this work do not account for surface undulations, while, in reality, the surface roughness can vary randomly between each electrode. This limitation is mitigated by the fact that the sensor capacitance shows low sensitivity to the electrode thickness variation as well as the total thickness. Future work will account for advanced modeling of solder interconnects in a 3D layout which will help to improve predictions of metal resistivity. In addition to customized models, an online library needs to be created to allow the use of these models for rapid prototyping of larger sensor arrays for applications such as structural health monitoring; an idea similar to the current practice of foundry development kits available in conventional CMOS processes. The current work thus demonstrates an environmentally friendly additive fabrication method for touch sensors and develops a model that can predict the sensor behavior as a function of variables such as the interdigitated geometry and the surrounding medium. The results from this work can be used for design, low-cost manufacture, and integration of such sensors into electronic devices.

## 7. Conclusions

In this paper, we present the design, an additive manufacturing method, and electromagnetic simulations of an interdigitated capacitive touch sensor. The study revealed several important aspects of the touch sensor behavior as below:

- The Aerosol Jet micro-additive printing allowed the fabrication of sensors with an electrode dimension down to about  $45 \mu\text{m}$  and a native capacitance of a 1–5 pF. Characterization of the printed sensor using SEM and AFM studies showed that the sensor electrodes have high thickness variation and a rough surface, but a low sensor native capacitance variation within 8%. The sensor capacitance increased with the interdigitated region length.
- A 3-D electromagnetic model was developed to simulate the touch sensors and find the electric field distribution for the geometries studied in the paper. The simulations showed a reasonable agreement with the experimental values for the native capacitance of the sensor (within 12.5%).

- c) The simulations also revealed the physical range of the sensor action out of the plane of the electrodes to be about a millimeter for the geometries used in the current study indicating that this device can also be used as a proximity sensor under certain conditions.
- d) The simulations further showed that the sensor capacitance was relatively insensitive to the thickness of the sensor electrodes. This explained the experimental observation of a low capacitance variation in spite of the high variation in the sensor electrode thickness. Lastly, the simulations revealed that the width, W, of the electrode as a fraction of the electrode pitch ( $W + G$ ) is one of the key variables determining the sensor capacitance and that this dependence is divided into three separate regions. In the first region, the sensor capacitance increases rapidly until W is about 2.5% of the pitch ( $W + G$ ). The capacitance then increases at a slower rate until W is about 90% of the pitch ( $W + G$ ). As W approaches the pitch ( $W + G$ ), i.e. when the gap between the electrodes is small, the capacitance increases rapidly again.

## Acknowledgements

This work was supported by RP's and SG's start-up funds at WSU. We acknowledge the help from Mr. Abhishek Gannarapu, Dr. Arda Gozen, Mr. John Yates and Mr. Scott Hansen at WSU. We also thank the anonymous reviewers for their valuable comments.

## Appendix A. Supporting information

Supporting information associated with this article can be found, in the online version, at <http://dx.doi.org/10.1016/j.sna.2016.07.014>.

## References

- [1] Gartner Report at <http://www.gartner.com> 2014.
- [2] J. Gubbi, R. Buyya, S. Marusic, M. Palaniswami, Internet of Things (IoT): a vision, architectural elements, and future directions, *Future Gener. Comput. Syst.* 29 (2013) 1645–1660.
- [3] R.D. Ponce Wong, J.D. Posner, V.J. Santos, Flexible microfluidic normal force sensor skin for tactile feedback, *Sens. Actuators A: Phys.* 179 (2012) 62–69.
- [4] M.M. Rodgers, V.M. Pai, R.S. Conroy, Recent advances in wearable sensors for health monitoring, *IEEE Sens. J.* 15 (2015) 3119–3126.
- [5] S. Khan, L. Lorenzelli, R.S. Dahiya, Technologies for printing sensors and electronics over large flexible substrates: a review, *IEEE Sens. J.* 15 (2015) 3164–3185.
- [6] B. Paul, R. Panat, C. Mastrangelo, D. Kim, D. Johnson, Manufacturing of Smart Goods: Current State, Future Potential and Research Recommendations, *ASME J. Micro and Nano-Manuf.* (2016), <http://dx.doi.org/10.1115/1.4033968>, In Press.
- [7] Y. Hotta, Y. Zhang, N. Miki, A flexible capacitive sensor with encapsulated liquids as dielectrics, *Micromachines* 3 (2012) 137–149.
- [8] A.P. Sample, D.J. Yeager, J.R. Smith, A capacitive touch interface for passive RFID tags, *IEEE International Conference on RFID* (2009) 103–109.
- [9] D.P. Cotton, I.M. Graz, S.P. Lacour, A multifunctional capacitive sensor for stretchable electronic skins, *IEEE Sens. J.* 9 (2009) 2008–2009.
- [10] A.D. Mazzeo, et al., Paper-based, capacitive touch pads, *Adv. Mater.* 24 (2012) 2850–2856.
- [11] R.-Z. Li, A. Hu, T. Zhang, K.D. Oakes, Direct writing on paper of foldable capacitive touch pads with silver nanowire inks, *ACS Appl. Mater. Interfaces* 6 (2014) 21721–21729.
- [12] Jacob J. Adams, E.B. D. Thomas F. Malkowski, Michael J. Motala, Bok Yeop Ahn, Ralph G. Nuzzo, Jennifer T. Bernhard, Jennifer A. Lewis, Conformal printing of electrically small antennas on three-dimensional surfaces, *Adv. Mater.* 23 (2011) 1335–1340, <http://dx.doi.org/10.1002/adma.201003734>.
- [13] Mohsin I. Tiwana, Stephen J. Redmond, Nigel H. Lovell, A review of tactile sensing technologies with applications in biomedical engineering, *Sens. Actuators A: Phys.* 179 (2012) 17–31.
- [14] D. Dimos, B.H. K., P. Yang in International Symposium on Advanced Packaging Materials.
- [15] E. MacDonald, R. Salas, D. Espalin, M. Perez, E. Aguilera, D. Muse, R. Wicker, 3D printing for the rapid prototyping of structural electronics, *IEEE Access* 2 (2014) 234–242.
- [16] A. Mette, P. Richter, M. Hörteis, S. Glunz, Metal aerosol jet printing for solar cell metallization, *Prog. Photovoltaics Res. Appl.* 15 (2007) 621–627.
- [17] C. Yang, E. Zhou, S. Miyanishi, K. Hashimoto, K. Tajima, Preparation of active layers in polymer solar cells by aerosol jet printing, *ACS Appl. Mater. Interfaces* 3 (2011) 4053–4058.
- [18] C. Goth, S. Putzo, J. Franke, in: *Electronic Components and Technology Conference (ECTC)*, 2011 IEEE 61st, 1211–1216 (IEEE).
- [19] H. Yang, M.T. Rahman, D. Du, R. Panat, Y. Lin, 3-D printed adjustable microelectrode arrays for electrochemical sensing and biosensing, *Sens. Actuators B: Chem.* 230 (2016) 600–606.
- [20] B. Andò, S. Baglio, S. La Malfa, G. L'Episcopo, All inkjet printed system for strain measurement, *IEEE Sens. Conf.* (2011) 215–217.
- [21] B. Andò, S. Baglio, All-inkjet printed strain sensors, *IEEE Sens. J.* 13 (2013) 4874–4879.
- [22] M.T. Rahman, L. Renaud, M. Renn, D. Heo, R. Panat, Aerosol based direct-write micro-additive fabrication method for sub-mm 3-D metal-dielectric structures, *J. Micromech. Microeng.* 25 (2015) 107002.
- [23] J.A. Paulsen, M. Renn, K. Christenson, R. Plourde, Future of instrumentation international workshop (FIIW), *IEEE* (2012) 1–4.
- [24] K. Park, D. Seo, J. Lee, Conductivity of silver paste prepared from nanoparticles, *Colloids Surf. A: Physicochem. Eng. Aspects* 313–314 (2008) 351–354.
- [25] A.F. Peterson, S.L. Ray, R. Mittra, *Computational Methods for Electromagnetics*, vol. 2, IEEE press, New York, 1998.
- [26] W.C. Gibson, *The Method of Moments in Electromagnetics*, CRC press, 2014.
- [27] J. Freer, J. Morris, Microstructure and creep of eutectic indium/tin on copper and nickel substrates, *J. Electron. Mater.* 21 (1992) 647–652.
- [28] A. Liu, et al., A combined theoretical and experimental study for silver electroplating, *Sci. Rep.* 4 (2014) 3837, <http://dx.doi.org/10.1038/srep03837>.
- [29] P. Kejík, C. Kluser, R. Bischofberger, R.S. Popovic, A low-cost inductive proximity sensor for industrial applications, *Sens. Actuators A: Phys.* 110 (2004) 93–97.
- [30] A.Z. Capri, P.V. Panat, *Introduction to Electrodynamics*, Alpha Science Int'l Ltd., 2002.
- [31] G. Boothroyd, Product design for manufacture and assembly, *Comput.-Aided Des.* 26 (1994) 505–520.
- [32] G.S. May, C.J. Spanos, *Fundamentals of Semiconductor Manufacturing and Process Control*, John Wiley & Sons, 2006.

## Biographies

**Md Taibur Rahman** is a PhD student in the School of Mechanical and Materials Engineering at the Washington State University, Pullman. He received his MS degree from the University of Texas at El Paso and BS degree from the Chittagong University of Engineering and Technology, Bangladesh. He has several papers to his credit in the areas of ceramics and additive manufacturing.

**Arya Rahimi** is a PhD student in the School of Electrical Engineering and Computer Science at the Washington State University, Pullman. He received his BS from Washington State University in 2013. His research is focused on bio-signal acquisition and processing techniques as well as design and characterization of 3D printed electronics.

**Subhanshu Gupta** is an assistant professor in the School of Electrical Engineering and Computer Science at the Washington State University, Pullman. He received the B.E. degree from the National Institute of Technology, Trichy, India, in 2002, and the M.S. and Ph.D. degrees from the University of Washington, Seattle, WA, USA, in 2006 and 2010, respectively. From 2011 to 2014, he was a Staff Design Engineer in RFIC/Mixed Signal group at Maxlinear Inc., Irvine. At Maxlinear, Subhanshu worked on a broadband transceivers for cable/satellite systems. From 2015, he has been an Assistant Professor of Electrical Engineering at Washington State University where he is supervising over Systems-on-Chip Lab. Dr. Gupta has been the recipient of the Analog Devices Outstanding Student Designer Award in 2008 and IEEE RFIC Symposium Best Student Paper Award in 2011. His current research interests include broadband reconfigurable architectures for wireless backhaul and millimeter-wave applications, signal and image processing paradigms for heterogeneous networks and sensors, flexible electronic circuits for smart goods and ultra-thin substrate IC design for low-power sensors.

**Rahul Panat** is an associate professor in the School of Mechanical and Materials Engineering at the Washington State University, Pullman. He received his MS in Mechanical Engineering from the University of Massachusetts, Amherst in 1999 and his PhD from the University of Illinois at Urbana-Champaign in Theoretical and Applied Mechanics in 2004. He worked at Intel's manufacturing R&D from 2004–2014 before joining WSU in Fall 2014. At Intel, Dr. Panat worked on lead-free conversion of flash memory processors, fine line-space PCB development, and ceramic capacitors and their integration in IC chips. Dr. Panat also worked as an adjunct faculty at the Arizona State University from 2012–2014 in the area of flexible Li-ion batteries. Dr. Panat leads the Advanced Manufacturing Laboratory at WSU with concentration in the areas of printed and flexible electronics, packaging, 3-D mm wave antennas, and Li-ion batteries. Dr. Panat is the recipient of several awards including a Gold Medal from MRS, and several Divisional Recognition Awards at Intel, including one for his work on the first halogen-free chip.

# Appendix A: Supporting Information

## S-1: Modeling and Simulation of Sensor in Un-Touched State

Figure S2 shows the substrate model used for the printed capacitor sensors with the interdigitated region length of 5 mm in Momentum ADS®. A 1 mm thick glass substrate was used with a 1  $\mu\text{m}$  thick Metal1 (M1) (Ag nanoparticles) extending vertically on top of the glass substrate. Air was used as the surrounding dielectric medium for initial simulations (Fig. S2-a) with more complex media used to model touch sensitivity (Fig. S2-b). Table S1 lists various parameters for the substrate model such as metal resistivity, thickness and dielectric permittivity. Figure S2-c depicts the top-down layout views of the capacitor including interconnect and pad structures along with dimensions used for modeling. Long interconnect lengths were used to isolate any pad parasitic capacitances from the sensor. The sensor pads were simulated with 1  $\mu\text{m}$  thickness in contrast to the fabricated thickness of 4  $\mu\text{m}$  to avoid maintaining two separate layouts with different metal thicknesses. Simulations with 4  $\mu\text{m}$  thickness for the entire structure showed only a marginal increase (<0.05%) in capacitance at < 1 MHz thereby allowing the sensor pads to be simulated with 1  $\mu\text{m}$  thickness without any significant effect. The current layout did not include 3D electromagnetic (EM) components which were added later for the EMPro simulation. A Hammerstead surface roughness parameter in Momentum ADS® modeled the surface undulations on the metal electrodes observed from the AFM images, and showed a negligible effect on capacitance and quality factor below 100 MHz. The EM mesh in Momentum ADS® was configured with the “edge mesh” option enabled, a density of 200 cells/wavelength, and a mesh frequency set to 1 GHz. An image of the EM mesh for the sensor is shown in Fig. S3. While simulating the touch sensor, the capacitor ports were set such that Momentum ADS® removes any fringe capacitance at the edge of the metal thus avoiding that the parasitics being counted twice. Capacitance was then derived from the simulated *S-parameters* using the following custom Momentum ADS® equations<sup>1</sup>:

$$Z = \text{stoz}(s, 50) \quad (1)$$

$$Z_{in} = Z(1,1) - \frac{Z(1,2)Z(2,1)}{Z(2,2)} \quad (2)$$

$$C = \text{imag}\left(\frac{1}{2\pi f Z_{in}}\right), \quad (3)$$

where “stoz” is a custom function to convert *S-parameter* data to *z*-parameter data, and “imag” returns the imaginary part of a complex number.

## S-2: Modeling and Simulation of Sensor in Touched State

The touch sensitivity of the capacitive sensors was further simulated through a model developed for human touch in Momentum ADS® (Fig. S2-b). A 2  $\mu\text{m}$  layer of air was left above M1 to simulate a possible gap caused by the plastic layer covering the 0.5 – 2 micron high sensor electrodes above the substrate. A 100  $\mu\text{m}$  thick plastic film above the air gap modeled the insulator between the thumb and the sensor. This insulator was used as a buffer between the human thumb and the sensor to avoid shorting the structure and contaminating the electronics. The thumb dielectric consisted of multiple layers of different dielectric properties. At the frequencies of interest, all the tissues were expected to affect the dielectric, including those for hypodermis, dermis, and epidermis. However, the thickness of these layers varies considerably (e.g. hypodermis from 0.3-3 mm, dermis 0.3-3 mm, and epidermis 0.5-1.5 mm)<sup>2</sup>, resulting in

considerable difference in the effective dielectric from person-to-person and even for the same person contacting the sensor at different times (due to factors such as difference in the applied pressure). Here, we modeled the dry human thumb as a single dielectric medium with relative permittivity,  $\epsilon_r=40^2$ . The final layer was modeled as M2 which grounded the human thumb. The layout with metal layers and interlayer dielectric materials was same as that shown in Fig. S2-c. A 3-port *S-parameter* simulation was carried out to characterize the dry thumb test case.

### **S-3: 3D E-Field Simulation in ADS EMPro**

A 3D electric field (E-field) estimation was done through EMPro® for the model imported from Momentum ADS®. Figures S4-a, b, and c show the capacitor structure in EMPro®. Boundary boxes are placed at the edge of the structure to define 3D simulation space. The Finite Element Method (FEM) solver option was used in EMPro® to achieve faster convergence. The E-field was estimated both in-plane and out-of-plane directions as shown in Figs. 6-a, b, respectively, using EMPro® near-field planar surface sensor features.

### **S-4: Internal Circuit Schematic**

Figure S6 shows the internal circuit schematics of the LCR meter referenced from Agilent<sup>27</sup> when a Device Under Test (DUT), the capacitive touch sensor in this case, is connected to the terminals. An active-feedback circuit called as “Auto-Balancing Bridge (ABB)” (Fig. S6) is used to model one end of the DUT as a virtual ground and calibrate the current during the initial calibration steps accounting for any series resistance (solder or lead resistance). As the capacitor sensor is brought in vicinity to external parasitics (human thumb for example), the ABB tries to auto-adjust the current through the virtual ground by changing the amplifier gain to maintain the node  $L_p$  at virtual ground. The negative feedback causes the circulating AC current to reduce resulting in a ‘false’ decrease in measured capacitance rather than an increase as expected. Thus, once calibrated, the LCR meter can’t be used to measure a touch sensitivity on the fly. This observation was further verified in the lab on the LCR meter. To overcome this issue, the capacitance is measured directly using the RC time constant observed on an oscilloscope, with the measured results shown in Figs. 7-b, c, d.

## **REFERENCES**

- 1 Agilent. Advanced Design System documentation for Momentum. . <http://cp.literature.agilent.com/litweb/pdf/ads2008/mom/ads2008/index.html> (2008).
- 2 Nanzer, J. A. *Microwave and millimeter-wave remote sensing for security applications*. (Artech House, 2012).

**Table S1:** Electrical properties of the touch sensor used for the electromagnetic simulations

Parameter	Value
<b>Substrate Permittivity</b>	3.9
<b>Plastic Permittivity</b>	3.7
<b>Dry Thumb Permittivity</b>	40
<b>Substrate Thickness</b>	1000 $\mu\text{m}$
<b>Metal 1 and Metal 2 Thickness</b>	1 $\mu\text{m}$
<b>Air Gap Between Plastic and Metal 1</b>	2 $\mu\text{m}$
<b>Plastic Thickness</b>	100 $\mu\text{m}$
<b>Dry Skin Thickness</b>	1000 $\mu\text{m}$
<b>Metal 1 and Metal 2 Resistivity</b>	3.23 $\mu\Omega\cdot\text{cm}$

**Table S2:** Rise time constant and fall time constant for the plots in Fig. 7

Interdigitated Region Length (mm)	$\tau_{\text{rise\_touched}}$	$\tau_{\text{rise\_untouched}}$	$\tau_{\text{fall\_touched}}$	$\tau_{\text{fall\_untouched}}$
	( $\mu\text{s}$ )	( $\mu\text{s}$ )	( $\mu\text{s}$ )	( $\mu\text{s}$ )
1.5	0.426	0.233	0.355	0.214
3	0.454	0.254	0.436	0.245
5	0.603	0.337	0.541	0.318

**Table S3:** Data used to plot Fig. 8

Interdigitated Region Length, (mm)	Number of Electrode Pairs	State	Capacitance from Simulations, (pF)	Capacitance from experiments (Mean) (pF)	Capacitance from experiments, (Std Dev) (pF)	Experimental Method
1.5	20	Untouched	1.98	1.97	0.18	LCR Meter
1.5	20	Touched	3.99	3.91	0.23	Oscilloscope*
3	20	Untouched	3.05	3.28	0.13	LCR Meter
3	20	Touched	5.86	7.87	1.38	Oscilloscope*
5	20	Untouched	4.52	5.4	0.13	LCR Meter
5	20	Touched	8.38	10.66	1.18	Oscilloscope*
3	8	Untouched	1.66	1.33	-	LCR Meter
3	14	Untouched	2.36	-	-	-

\* The RC time constants for the touched and untouched states were directly measured using an oscilloscope to obtain the ratio of the capacitance in the touched state to that in the untouched state (see section 5). This ratio along with the untouched capacitance from the LCR meter gave the experimental value of the capacitance in the touched state.

**Figure S1:** Image of the Aerosol Jet micro-additive manufacturing machine used to fabricate the sensors in the current study.

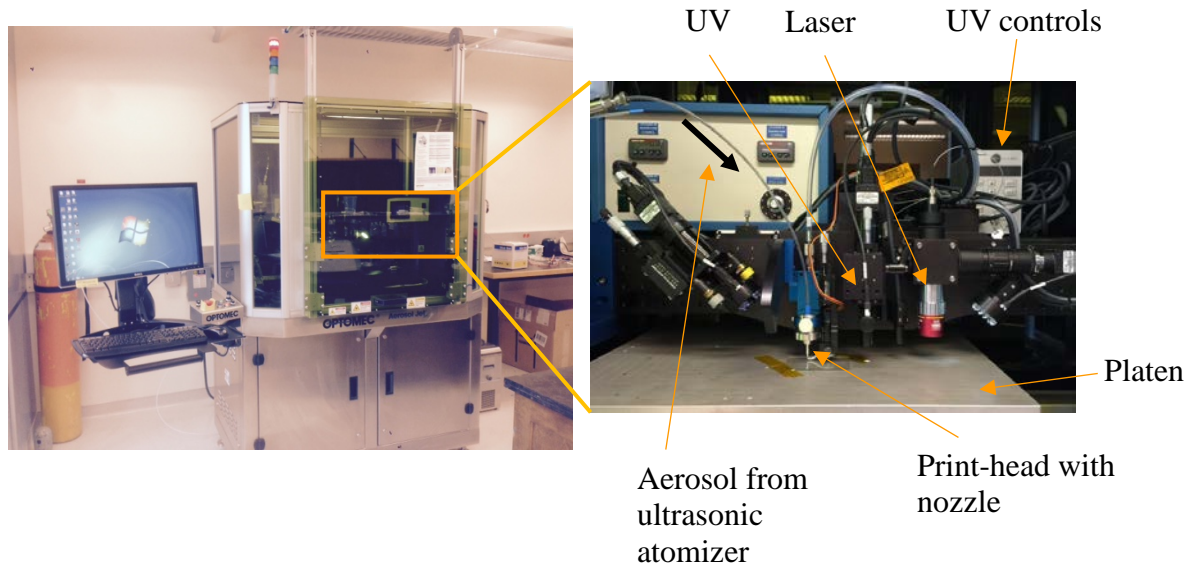


**Figure S2:** Sensor modeling using Momentum ADS® showing a) model to simulate the sensor in untouched state, b) model to simulate a dry human thumb touching the sensor, c) top layout view of the sensor with dimensions used for the simulations in the untouched and untouched cases.

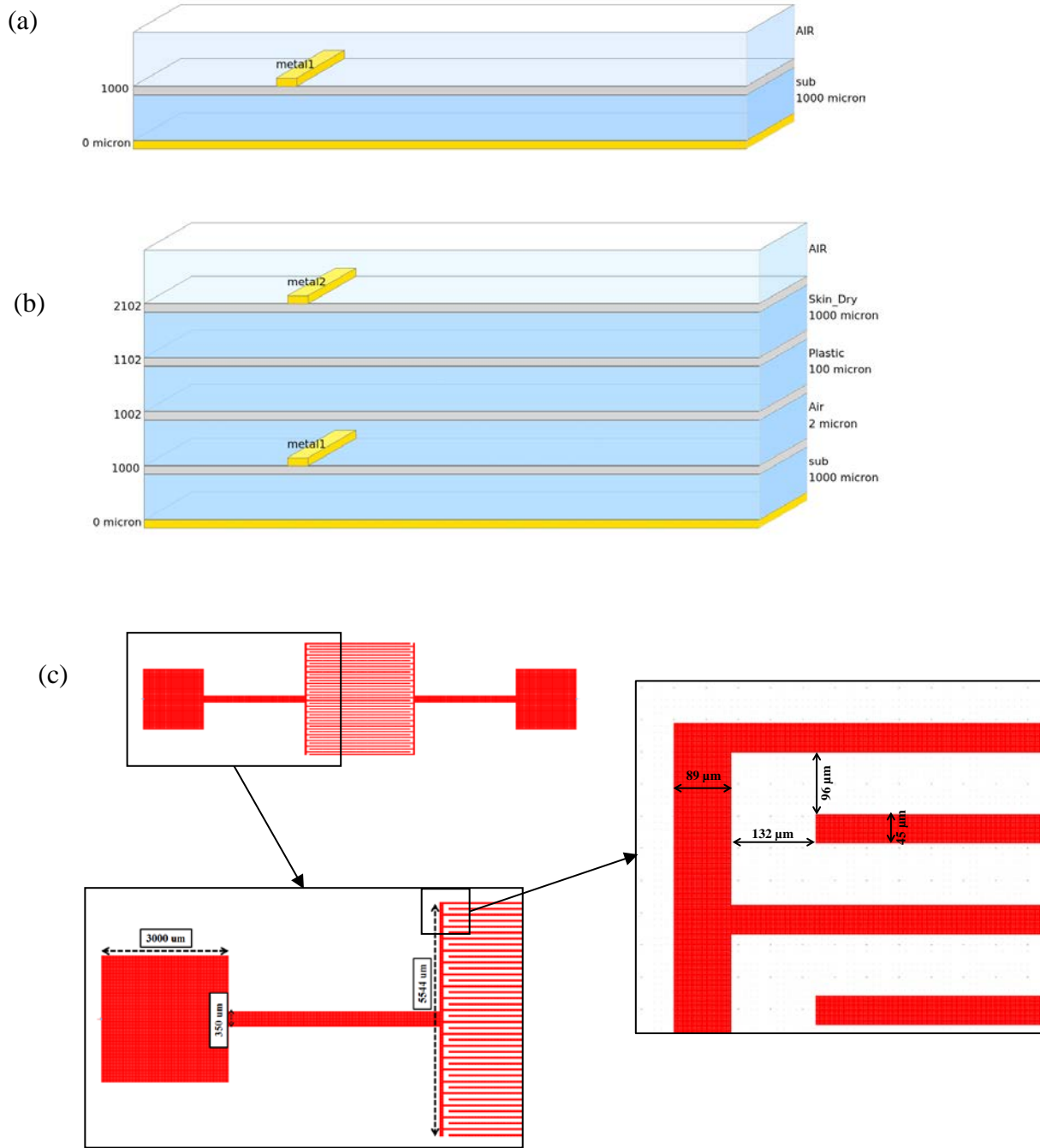


**Figure S3:** Electromagnetic (EM) mesh generated by the software for sensor structure with ~200 cells/wavelength at a mesh frequency set to 1GHz in Momentum ADS®.

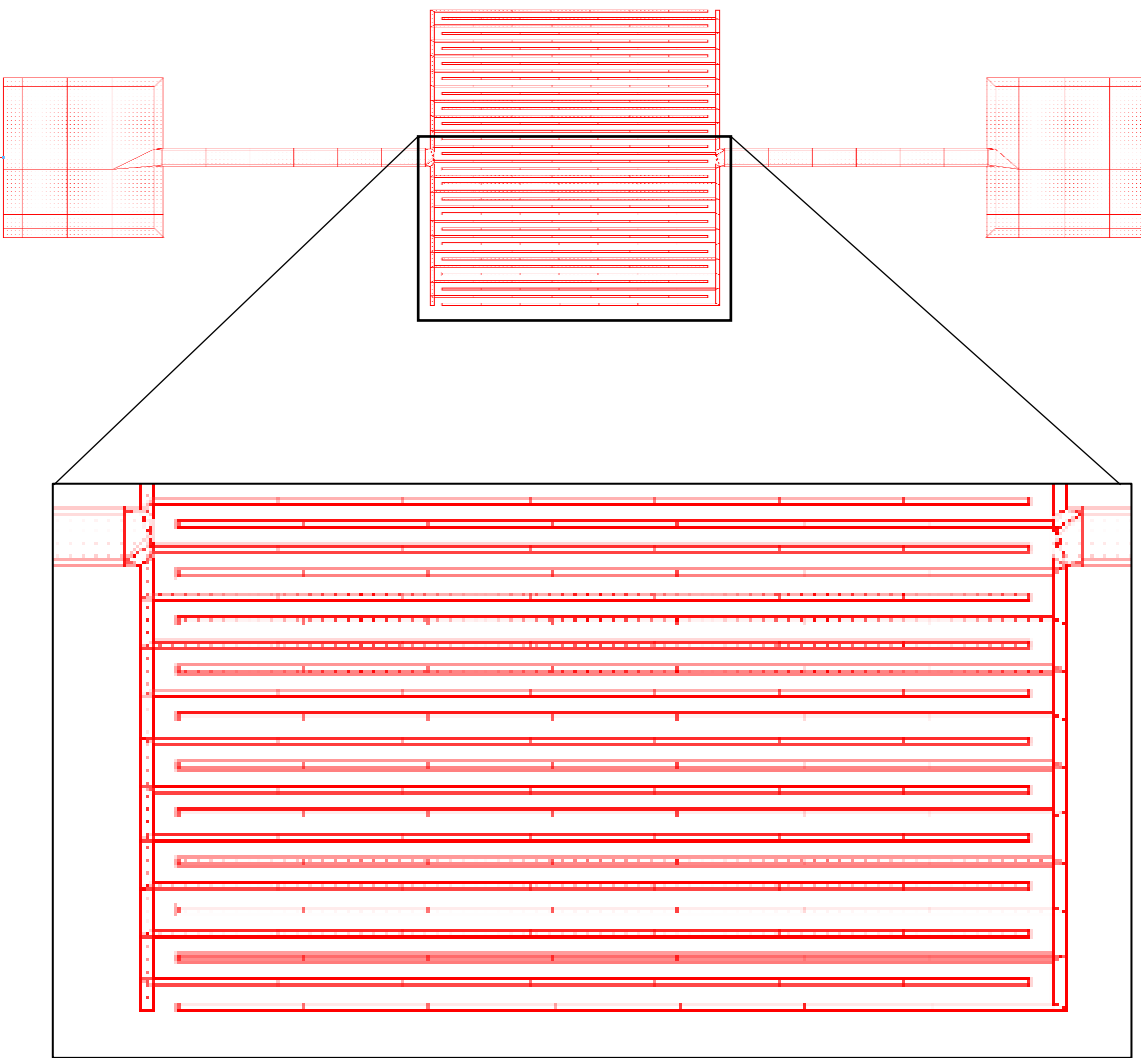


**Figure S4:** Simulation of the electric fields of the capacitive sensor. a) EMPro imported structure. b) EMPro perpendicular planar sensor. c) EMPro planar sensor 'Cutting' into the structure in the x direction.

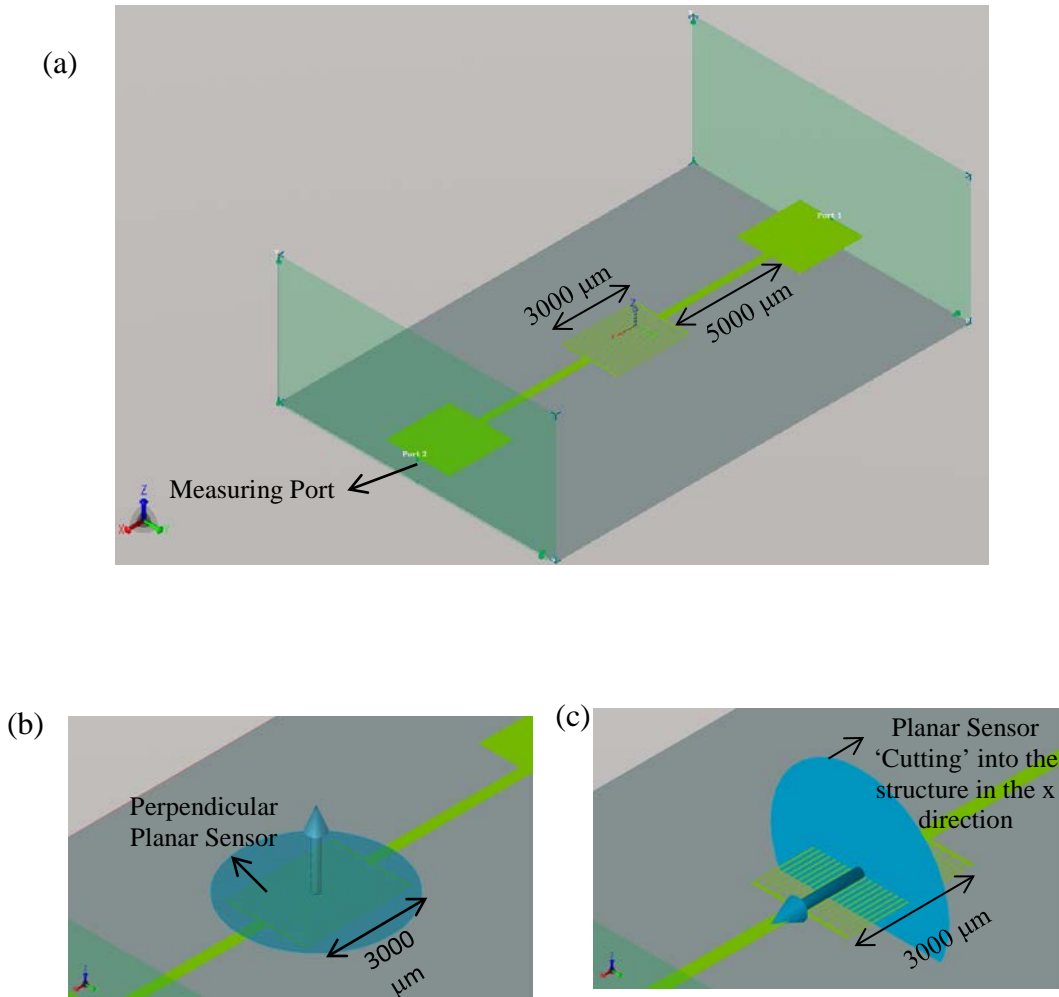


**Figure S5:** Set-up to measure interdigitated touch sensor capacitance.

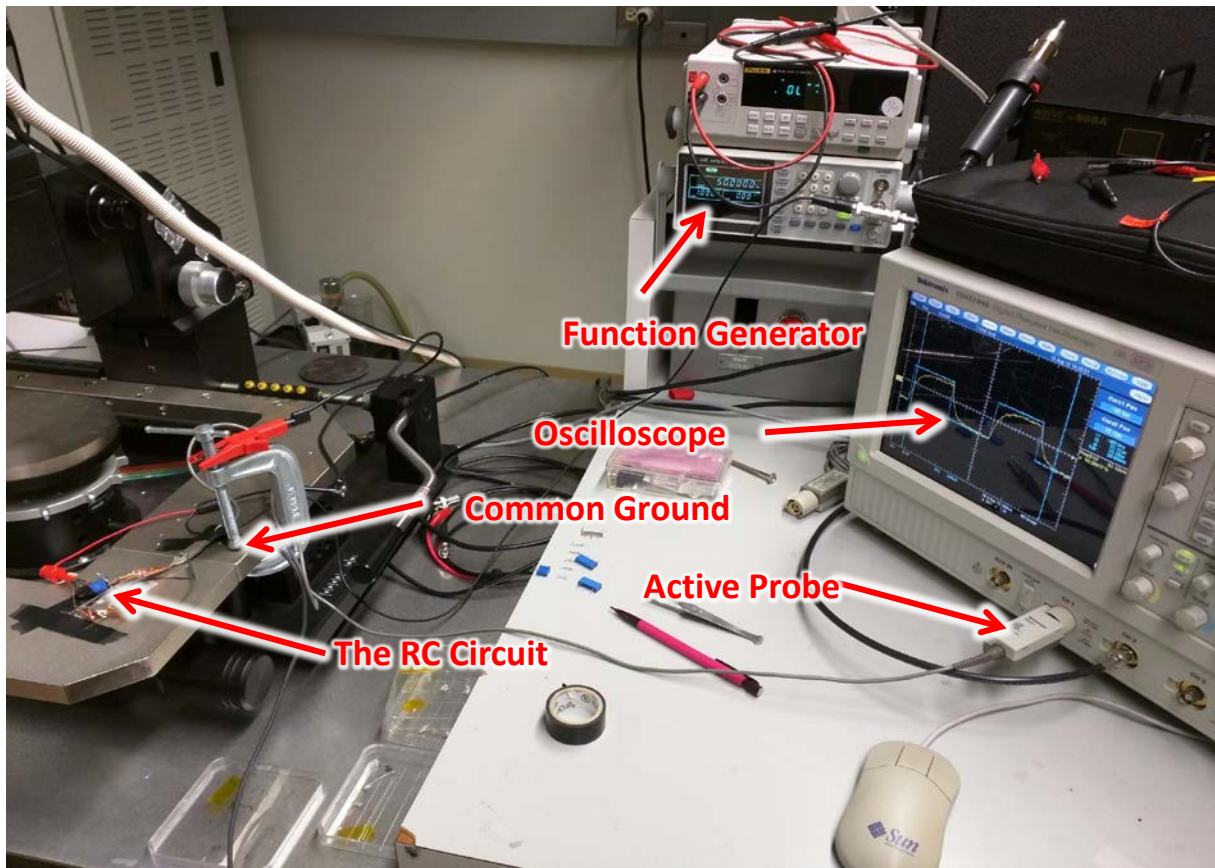


**Figure S6:** Internal circuit schematics of the LCR meter when a Device Under Test (DUT), i.e., the capacitive touch sensor, is connected to the terminals.

